Road Surface Conditions Identification via H α A Decomposition and Its Application to mm-Wave Automotive Radar

Bouwmeester, Wietse; Fioranelli, Francesco; Yarovoy, Alexander G.

DOI
10.1109/TRS.2023.3286282

Publication date
2023

Document Version
Final published version

Published in
IEEE Transactions on Radar Systems

Road Surface Conditions Identification via $H\alpha A$ Decomposition and Its Application to mm-Wave Automotive Radar

Wietse Bouwmeester, *Graduate Student Member, IEEE*, Francesco Fioranelli, *Senior Member, IEEE*, and Alexander G. Yarovoy, *Fellow, IEEE*

***Abstract*— A novel approach based on the entropy-alpha-anisotropy decomposition, also known as the $H\alpha A$ decomposition, for the recognition of road surface conditions using automotive radar is presented. To apply the $H\alpha A$ decomposition to automotive radar data, a dedicated signal processing pipeline has been developed. To investigate its effectiveness, fully polarimetric measurements of surface scattering were performed in lab conditions as well as outdoors on actual road surface material under various conditions. A high-level analysis using the Euclidean distances between cluster centroids and the standard deviations of the H, α, and A features is performed, and it is shown that the proposed pipeline can provide an opportunity for classification of road surfaces, leading to enhanced road safety. Finally, the effect of neglecting the cross-polar components of the fully polarimetric measurements is considered. It is shown that in this case, the A feature cannot be used anymore. Despite this, the H and α features can still be used and several road surface conditions can still be distinguished from each other at the cost of less separation between the classes, thus leading to a trade-off between classification accuracy and radar system cost/complexity.**

***Index Terms*— Automotive, radar, polarimetry, road surface condition, recognition, classification, $H\alpha A$ decomposition.**

I. Introduction

In an effort to increase on-road safety, more and more vehicles are being equipped with advanced radar systems. These radar systems are usually employed to detect, and in many cases also classify, other road users and obstacles. Automotive radar systems for the 24 GHz band are being phased out and a transition to the new 77 GHz band has largely been completed [1], [2]. This has presented a new opportunity to use these radar systems to observe road surface conditions in front of the vehicle. Namely, the rough structure of road surfaces results in more power that is scattered back to the radar sensor in the 77 GHz band compared to the 24 GHz band due to the shorter wavelength.

On the one hand, this causes the radar to detect more clutter. However, instead of considering these returns as clutter, they can also be used in an effective way to estimate the road surface conditions in front of the vehicle, e.g. whether the road surface is dry, wet or icy, or covered with potentially slippery material. Information on the road surface condition up ahead is crucial for improving driving safety systems such as the anti-lock breaking system and electronic stability control. If these systems can be provided with an estimation of the road surface conditions up ahead, they could already be tuned closer to the right operating point to minimise braking distance and maximise vehicle stability [3]. In the case of fully-autonomous driving, dangerous road surface conditions such as a patch of ice could be automatically steered around altogether.

Road surface classification has been investigated using conventional (single polarised) radar; a few notable examples of this can be found in [4], [5], [6], and [7]. In [5] and [6], convolutional neural networks are used on vertically polarised radar imagery of sandpaper and rough surface types, while in [4] the statistical distribution of vertically polarised backscattering from a number of road surface conditions was studied. Also in [7], surface classification was performed by fitting a Weibull distribution to the backscattered power and studying the resulting variation of the distribution parameters.

Polarimetric radar has the distinct advantage that the full polarimetric characteristics of the targets of interest are measured. As different targets have different polarimetric characteristics, the extra information provided by this ability can be used for classification. This is for example routinely used in the context of remote sensing, target classification, and weather radar [8], [9], [10]. Polarimetric radar has also been proven to be effective in the characterization of targets in automotive scenarios [11], [12].

Surfaces have distinctive polarimetric scattering behaviours depending on surface roughness (i.e., parameters such as the root mean square height and correlation function) and material properties [13], [14]. This makes polarimetric radar a great candidate to exploit different scattering behaviours for road surface classification purposes in the automotive context.

Previous publications have considered using polarimetric features for road surface identification [15], [16], [17]. In that research, simple polarimetric features such as the co-polar and cross-polar backscattering ratios have been utilised. More specifically, [15] and [16] consider the use of polarisation ratios. These include co-polarised horizontal and vertical backscattering ratios, as well as cross-polar backscattering ratios. In [17], the mean powers in the co- and

Manuscript received 20 January 2023; revised 28 April 2023; accepted 9 June 2023. Date of publication 14 June 2023; date of current version 23 June 2023. *(Corresponding author: Wietse Bouwmeester.)*

The authors are with the Microwave Sensing Signals and Systems (MS3) Group, Department of Microelectronics, Delft University of Technology (TU Delft), 2628 CD Delft, The Netherlands (e-mail: w.bouwmeester@tudelft.nl; f.fioranelli@tudelft.nl; a.yarovoy@tudelft.nl).

Digital Object Identifier 10.1109/TRS.2023.3286282

cross-polarised channels were investigated, as well as their standard deviations.

While effective, these features are relatively simple and do not necessarily exploit the whole amount of rich information that can be inferred from more complex polarimetric decompositions. In this work, the polarimetric approach is taken to the next level by introducing a novel processing pipeline specifically designed for automotive radar based on the $H\alpha A$ decomposition for road surface identification purposes.

The $H\alpha A$ decomposition is known from the field of remote sensing and Earth observation and has been successfully applied to data from both synthetic aperture radar [8] and conventional radar [18]. Also, it has been demonstrated that the entropy feature of this decomposition is effective for road surface classification [19].

The $H\alpha A$ decomposition operates on the statistical properties of the polarimetric signatures of an object to extract the H, α, and A features. Their importance relates to the fact that they can model and capture the physical scattering processes occurring within said object. For example, in the case of Earth observation with synthetic aperture radar, scattering that is characterised by an entropy value, denoted H, between 0.5 and 0.9 and an α value between 40° and 50° corresponds to scattering from anisotropic particles, while scattering with an entropy value between 0 and 0.5 and an α value between 0° and 42.5° corresponds to Bragg surface scattering [20].

However, the $H\alpha A$ decomposition as applied in the aforementioned applications, cannot be used directly in automotive radar. This is due to differences in observation geometry and platform movement. Therefore, to investigate the effectiveness of the proposed approach based on $H\alpha A$ features for road surface identification purposes, a novel processing pipeline is proposed to compute these features in the automotive scenario. The proposed pipeline compensates for the strongly varying distance between observed road surface returns that occurs due to the observation geometry of the automotive scenario, and proposes a new way of averaging of the scattering parameters for computing the coherency matrix.

Subsequently, measurement data of rough surface scattering in both lab conditions as well as outdoors on actual road surfaces has been collected using a vector network analyser. This data is then used to evaluate the proposed pipeline. Furthermore, using the measurement data, a polarimetric analysis is performed to investigate the performance impact on road surface identification when the cross-polar components are omitted. Notably in this case, if the cross-polar channels do not have to be measured, the ADCs (analogue to digital converters) of H and V channels do not have to be synchronised to each other thus making the hardware implementation easier. This means that such a radar could be constructed out of two separate single polarised radar systems. Also, since the backscattered power in the cross-polarised channels is usually much lower, requirements on the sensitivity of the radar system can be relaxed by leaving the cross-polar channels out. The results of the polarimetric analysis can then be used by radar designers to make a trade-off between performance and radar complexity leading to cost savings by leaving out cross-polar measurement capabilities.

In terms of contributions of this work, the obtained results show that the proposed pipeline is effective for road surface classification purposes and provides a robust alternative to a state-of-the-art classification technique based on polarimetric ratios. It has also been shown that the cross-polar components can be neglected, at the cost of reduced separation between clusters formed by the H, α, and A features of the considered classes of road surfaces.

The rest of the paper is organized as follows. In section II, an introduction to the $H\alpha A$ decomposition is provided. Section III describes the measurement setup and the measurement procedure whilst section IV describes the proposed pipeline for road surface identification. In section V the experimental results are presented and the paper concludes with section VI.

II. Theoretical Background

The $H\alpha A$ decomposition, introduced by Cloude and Pottier and originally developed for synthetic aperture radar, does not depend on knowledge of statistical distributions of targets, but assumes instead that there is a dominant average scattering mechanism and tries to find the characteristics of this scattering process [8]. The approach is based on Eigendecomposition of the so called coherency matrix T.

The computation of the H, α, and A features works as follows. The first step is to compute the target vector $\vec{k}$ as shown in (1), where S_{XX} refers to the co-polar scattering matrix element for X polarisation, measured in a XY polarisation basis [20]. In this equation, ^{T} indicates the transpose operator.

$$\vec{k} = \frac{1}{\sqrt{2}}\left[S_{XX} + S_{YY} \;\; S_{XX} - S_{YY} \;\; 2S_{XY}\right]^T \tag{1}$$

In this paper, a vertical/horizontal polarisation basis is used which leads to X corresponding to V polarisation and Y to H polarisation. Subsequently, using this target vector, the coherency matrix can be computed as shown in (2), where † indicates the conjugate transpose operator and the angle brackets indicate averaging.

$$T = \left\langle \vec{k}\vec{k}^\dagger \right\rangle \tag{2}$$

In synthetic aperture radar applications, this averaging is usually done over multiple cells in space where these cells contain the same (type of) object. However, for the proposed road surface classification approach in automotive scenarios, this averaging step can also be performed in a different manner as described in section IV-E.

Next, an Eigendecomposition is performed on the coherency matrix, resulting in 3 eigenvalues, denoted by λ_i, in order from larger to smaller, with λ_1 being the largest and λ_3 the smallest. The eigenvector corresponding to each eigenvalue λ_i is denoted by $\vec{u}_i$.

For each of the three eigenvalues, a pseudo-probability P_i can be computed as shown in (3) [20].

$$P_i = \frac{\lambda_i}{\sum_{k=1}^{3} \lambda_k} \tag{3}$$

Using the pseudo-probabilities corresponding to each eigenvalue, the entropy feature, denoted by H, can be computed as shown in (4) [8].

$$H = -\sum_{i=1}^{3} P_i \log_3 P_i \tag{4}$$

The entropy feature is a measure of how random the backscattering from a target is and whether or not there is one dominant scattering mechanism occurring, or if there are multiple dominant scattering mechanisms at play. When there is only one dominant scattering mechanism, the entropy is low and indicates deterministic scattering. When there are multiple dominant scattering mechanisms present, the observed scattering mechanism varies from observation to observation thus indicating a random scattering character which corresponds to a high entropy value.

Each eigenvector $\vec{u_i}$ can be represented in the form as shown in (5) [20].

$$\vec{u_i} = \begin{bmatrix} \cos\alpha_i e^{j\phi_i} \\ \sin\alpha_i \cos\beta_i e^{j(\delta_i+\phi_i)} \\ \sin\alpha_i \sin\beta_i e^{j(\gamma_i+\phi_i)} \end{bmatrix} \tag{5}$$

By using the identity shown in (5), the values of α_i, β_i, ϕ_i, δ_i, and γ_i can be computed for each eigenvector. Subsequently, the feature α can be found by computing a weighted average based on the pseudo-probabilities, as shown in (6) [20].

The angle α indicates the nature of the average scattering mechanism. For example, an α value of 0° relates to scattering from a spherical target whereas values of 45° and 90° correspond to scattering from anisotropic particles and dihedrals, respectively [20].

$$\alpha = \sum_{i=1}^{3} P_i \alpha_i \tag{6}$$

Finally, the anisotropy feature A can be computed as in (7).

$$A = \frac{\lambda_2 - \lambda_3}{\lambda_2 + \lambda_3} \tag{7}$$

The anisotropy feature A indicates how much of a role the eigenvector with the smallest eigenvalue has in the scattering process compared to the second-largest. This indicates the relative importance of the second scattering mechanism compared to the third scattering mechanism in the averaged response.

These three features can subsequently be used to make a classification of targets. In the case of synthetic aperture radar for Earth observation, the H and α features are often plotted against each other, creating a $H\alpha$-plane. This plane is subdivided in a number of sectors, where for example the sector that is delimited by $H < 0.5$ and $\alpha > 47.5°$ corresponds to scattering from a dihedral reflector and the sector delimited by $0.5 < H < 0.9$ and $\alpha < 40°$ corresponds to scattering from a random surface [20]. This direct relation to the underlying physical scattering mechanisms give the $H\alpha A$ decomposition a distinct advantage over simpler features such as the co-polar/cross-polar ratios, or mean values and standard deviations of polarimetric channels.

TABLE I
SETTINGS OF THE VNA AND FREQUENCY EXTENDERS

Centre Frequency	80 GHz
Bandwidth	10 GHz
Sweep Points	1001
Intermediate Frequency Bandwidth	10 kHz
Sweep Time	120.82 ms
Power	+16 dBm
Frequency Extender Attenuation	0 dB

The background theory presented in this section relates to the application of the $H\alpha A$ decomposition for Earth observation. Section IV discusses the proposed extra steps to apply this decomposition to the automotive scenario.

III. EXPERIMENTAL MEASUREMENTS

In this section the experimental setup is described, together with the measurement procedure in the laboratory, as well as the procedure for outdoor measurements.

A. Measurement Setup

Measurements were performed with a N5242A Vector Network Analyser (VNA) with two N5260-60003 frequency extenders to be able to operate in the band ranging from 75 to 85 GHz. The frequency extenders have WR-10 waveguide output sections, to which a 15 dBi gain dual-polarised horn antenna of type SAR-1532-122-S2-DP [21] was connected using the required waveguide sections. The vertically polarised port of the antenna was connected to the first port of the VNA, while the horizontal port was connected to the second. The settings of the measurement system are listed in table I.

A supporting structure was purposely built to which the frequency extenders and dual polarised horn were attached. This structure allows for controlling the orientation angle of the antenna in the vertical plane relative to the surface under test. The antenna orientation angle is defined as the angle the surface normal forms with the antenna broadside. In this way, the samples can be measured under various angles of incidence (Fig. 1).

B. Measurement Procedure

Measurements were performed in both indoor lab conditions and on real outdoor road surfaces. During the *lab measurements*, 3 types of sandpaper with different coarseness were used as surface samples: P24, P60, and P100. Here, P24 is the coarsest type of measured sandpaper while P100 is the finest. Sandpaper was selected as a suitable sample as it provides a surface of controlled roughness which is uniform over the whole sheet. The P24 type was selected as it was the coarsest sandpaper available on the market that is supplied as large sheets. The P100 type was chosen as a relatively smooth sample while the P60 type was used as an intermediate step. According to standards of the Federation of European Producers of Abrasives, P24 grit sandpaper has an average particle size of 764 μ m, while P60 and P100 types have average particle sizes of 269 μ m and 162 μ m respectively [22].

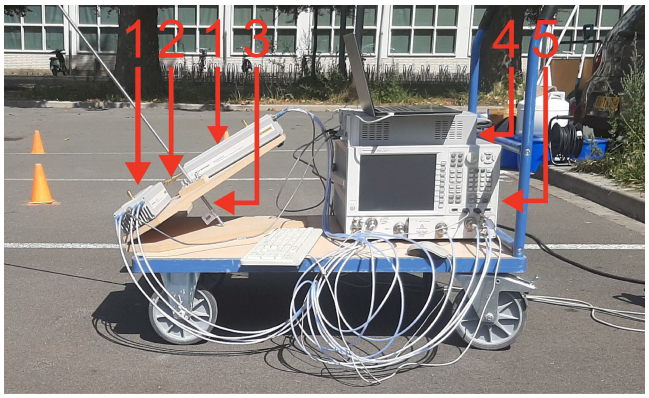

Fig. 1. Photograph of the setup as used for outdoor measurements to record surfaces-under-test at various angles of incidence. The setup consists of a VNA (5) with mm-wave extenders (1), powered by two power supplies (4), a dual-polarised horn antenna and corresponding waveguides (2), a support structure with a controllable antenna orientation angle (3).

The root mean square (RMS) height is approximately linearly dependent on average particle size as seen from [23], leading to an estimated RMS height of 220 μ m for the P24 type, while the reported RMS heights for the P60 and P100 types are 84 μ m and 41 μ m respectively. All sandpaper sheets measured at least 1.5 metres by 2 metres so that the -10 dB footprint of the antenna beam, for an antenna orientation angle of 60°, is well contained within the sample. The -10 dB antenna beam footprint was computed by using the procedure outlined in [24], and was found to be an oval of dimensions 95 cm by 44 cm.

In order to collect statistically independent samples, which are needed to compute the coherency matrix as described in section II, the sandpaper sheets were moved a few centimetres in between measurements to ensure that the surface within the antenna beam footprint would be uncorrelated with the previously measured area of the sheet. This is analogues to a car driving along a surface while performing measurements over time, resulting in measurements of uncorrelated surfaces for each time point. For each sandpaper sample, this procedure was repeated 50 times. To ensure stability of the measurements, every tenth measurement an additional measurement without sample was performed and compared to the background measurement done ten measurements before. These background measurements were also used for the background subtraction procedure as described in section IV-A.

For the measurements that took place outdoors, the measurement setup was placed on a trolley so that it could be moved easily as seen in Fig. 1. Several different road surface conditions were measured, namely asphalt under dry conditions, asphalt under wet conditions, and asphalt covered with gravel as one may encounter during roadworks (Fig. 2). All road surface conditions were measured for two antenna orientation angles. These were 60°, to replicate lab conditions and 90°, to replicate forward looking radar systems.

The measurement procedure for the *outdoors measurements* on asphalt was mostly the same as the lab measurements, except for moving the surface under test: in this case the measurement setup was moved instead. First, measurements were performed on asphalt under dry conditions. Subsequently, to emulate asphalt under wet conditions, buckets of water were poured over the previously measured area of asphalt. Every 10 measurements, more water was poured on the asphalt to keep the water layer consistent. Lastly, gravel, in the form of basalt split ranging from 2 to 8 mm in size was spread out over a dry part of asphalt and measured. As with the lab measurements, for each road surface condition and each antenna orientation angle, the backscattering from the asphalt road surface was measured in 50 uncorrelated spots to obtain representative statistical data.

The resulting data set from the in- and outdoor measurements has been made publicly available [25].

IV. Proposed Signal Processing Pipeline

The proposed processing pipeline comprises six parts. These are background subtraction, phase correction, time-domain transformation, footprint compensation, averaging and finally the $H\alpha A$ decomposition. The block diagram in Fig. 3 shows this processing pipeline schematically. The following sections describe each block in more detail.

A. Background Subtraction

A vector network analyser (VNA) measures S-parameters, which in the case of propagation measurements can be considered to be a ratio of a received electrical field over a transmitted electrical field. The received field can be decomposed due to the superposition principle in a contribution to the received electrical field by the sample, a contribution from the background, and a contribution from interactions between multiple scattering from the environment and targets. Therefore, the measured S-parameters can be written as shown in (8).

$$S_{measured} = \frac{E_{sample} + E_{background} + E_{interactions}}{E_{transmitted}} \tag{8}$$

In time domain, the contributions from the environment and targets follow after the main reflection of the calibration target (see later Fig. 5), and therefore these can be well separated and do not influence the calibration procedure further. Thus, the $E_{interactions}$ term can be assumed to be zero.

Therefore, by performing a measurement without any samples in the scene, the measured field is effectively purely the result of the background, which includes the response of the antenna and other static objects that may be present in the scene. In this way, only the ratio of $E_{background}$ and $E_{transmitted}$ is measured, which can be subtracted from measurements performed with samples present. This results in a removal of background effects and thus a clean S-parameter measurement of purely the surface-under-test. In Fig. 4, the result of this compensation procedure is shown. This figure shows the vertically polarised co-polar measurement results of a metal sphere placed at about 51 cm from the radar. The measurement results have been transformed from frequency domain, in which the S-parameters are naturally measured, to time domain so that a radar range profile is found. For more information on the time domain transformation, see section IV-C.

During the lab measurements, the sample could be easily removed and thus the background could be measured very

Fig. 2. Pictures of the measured road surface conditions. (a) Dry asphalt. (b) Wet asphalt. (c) Asphalt covered with gravel, consisting of basalt split with sizes ranging from 2 to 8 mm.

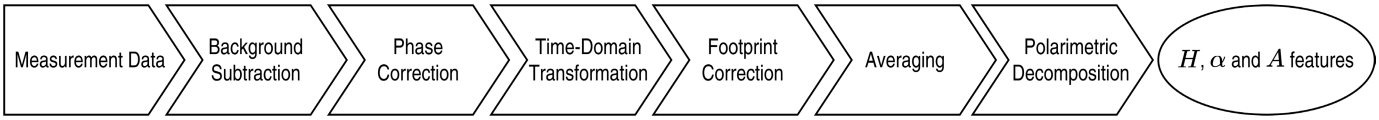

Fig. 3. Block diagram of the proposed signal processing pipeline for road surface identification for automotive applications using the H, α, and A features.

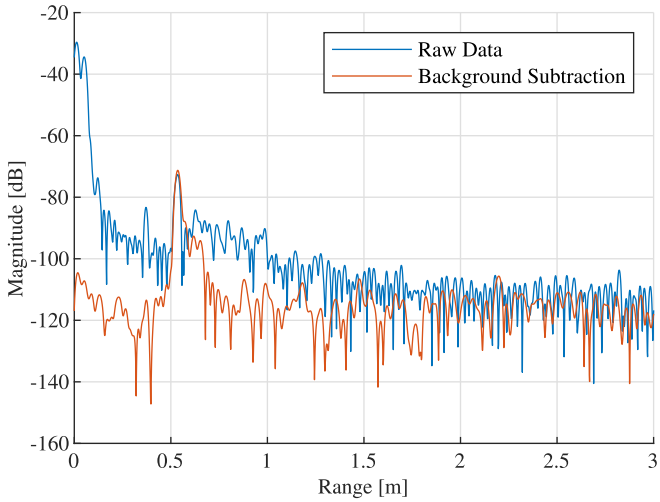

Fig. 4. Comparison of time domain transformed measurement data of the VV polarised channel before and after background subtraction. The target is in this case a metal sphere with a diameter of 3 cm and is located at a range of 0.51 m from the antenna.

accurately. However, for outdoor measurements, the road surface is the actual sample which obviously could not be removed. Therefore, to still be able to compensate for the antenna influences in the measurement results, the antenna was pointed towards the sky and a background measurement was performed. By subtracting this background from the measurement result, the scattering effects induced from the antenna response are suppressed.

B. Phase Correction

For measurements to which the $H\alpha A$ decomposition is to be applied on, special attention must be paid to the phase measured in each polarimetric channel. Namely, if the horizontally and vertically polarised channels are not balanced in length, a range-dependent phase error occurs. This may lead to a target appearing to be at a different range in one polarimetric channel than in another. Also, an absolute offset in phase between the channels can be present due to e.g., the way an antenna is fed, which likewise can distort the measurement results and the resulting feature values.

Although the measurements in this paper were performed using a symmetrical dual-polarised square horn antenna, the feeding network from the frequency extenders to the horn antenna is not exactly symmetrical and thus the phase of the measured scattering parameters needed to be corrected. Hence, a method to correct this phase difference was developed, based on measurements of a metal sphere.

A metal sphere approximates a point target and has the same radar cross section (RCS) for both horizontal and vertical co-polarised measurements due to its symmetry, while its cross-polar radar cross sections are 0 when the sphere is large compared to the wavelength. Therefore, a sphere with a diameter of 3 cm was chosen. Since the co-polar components of the sphere's RCS are equal, measurements of this reference target can be used to determine the phase offset of both horizontal and vertical channels, and can subsequently be used to compensate all four elements of the scattering matrix. These calibration measurements were performed before the start of each measurement session.

The first step in determining the phase offset is by applying time-domain gating to measurement data of the sphere [26]. This procedure filters out the contribution of scatterers other than the sphere that may be present in the scene, so that the sphere itself becomes the dominant target. As the sphere resembles a discrete target, the phase of the scattering parameters follows a linear decrease with frequency.

Subsequently, for each co-polarised channel, the phase is unwrapped and a function of form $\phi_{pp} = a_{pp} f + b_{pp}$ is fitted to the unwrapped phase where ϕ represents phase, f frequency and subscript p indicates the polarisation channel which can be H or V. Therefore, the parameter a corresponds to the phase gradient, which is dependent on the range to the target,

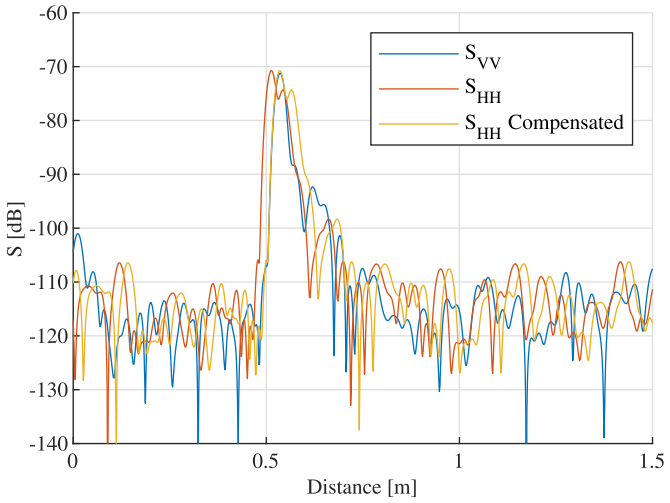

Fig. 5. Comparison of time domain transformed measurement data before and after the proposed phase correction procedure on the HH channel. The observed target is a metal sphere with a diameter of 3 cm, located at 0.51 m. Note that the double peak in the HH polarised channel is caused by a multipath reflection via the floor.

while b corresponds to an absolute phase offset within the channel.

In order for each channel to detect the sphere at the same range, the phase gradients of both co-polar channels need to be equal. Therefore, the vertically polarised channel is chosen as the reference channel and the phase gradient of the horizontally polarised channel is corrected so that equality of phase gradients is achieved by considering the difference between the gradients. Subsequently, the b_{pp}-component of the phase compensation is selected such that for each channel, the phase is 0 degrees at 75 GHz after compensation. This compensation is shown in mathematical form in (9) for the horizontal co-polarised channel.

$$S_{HH,compensated} = S_{HH,measured} e^{j(a_{VV}-a_{HH})f + jb_{HH}} \tag{9}$$

Due to the nature of the antenna setup used for these measurements, the cross-polar channels can be compensated as well. Namely, the electromagnetic radiation travels once through the V-polarised channel and once through the H-polarised channel. Therefore, the length of the cross-polar channels can be compensated using half of the compensation difference, as shown in (10). The VH channel can be compensated similarly by interchanging HV and VH. For the cross-polarised channels, the absolute phase term is set to zero as the cross-polar scattering coefficients of the spherical calibration target are zero.

$$S_{HV,compensated} = S_{HV,measured} e^{j\frac{(a_{VV}-a_{HH})}{2}f} \tag{10}$$

Fig. 5 shows the effect of the proposed phase correction procedure. It can be seen that the phase correction procedure shifts the peak resulting from the calibration target, so that in the HH-measurement this peak coincides with the peak in the VV-measurement. Furthermore, in Fig. 5, a second peak just after the main reflection of the target can be seen in the HH polarised channel. This peak is caused by a multipath reflection via the floor. This is due to the calibration measurements being performed with a 60° orientation angle while the calibration target was placed on a styrofoam block of 3 cm in height. This results in an extra path length of about 9 cm for the multipath reflection compared to the main reflection, and thus the second peak occurs at about 4.5 cm behind the main reflection. This multipath reflection manifests itself less significantly in the VV polarised channel, as the incidence angle of the multipath reflection is close to its Brewster angle.

C. Time-Domain Transformation

Since measurements are performed using a VNA, all S-parameter measurements are a function of frequency. To extract the range profile, they must be transformed to time domain. This can be done by means of discrete Fourier transformation. If necessary, a window function can be used such as a Kaiser window. Furthermore, in this step the range profile can also be interpolated using zero-padding in the frequency domain. In this instance, no window function and no zero-padding was employed in the $H\alpha A$ decomposition procedure.

D. Footprint Compensation

The S-parameters from the time-domain transformed measurements cannot directly be used to compute the coherency matrix. Namely, unlike in airborne or spaceborne synthetic aperture radar applications, the observed cells are not located at a comparable distance from the radar. Due to the geometry of the automotive scenario, large differences in propagation distance exist between backscattered contributions originating from the road surface close to the radar versus those from further away. Therefore, the free space attenuation will cause great differences in the magnitude of the backscattered contributions, which needs to be compensated for. Moreover, in the automotive scenario, the observed cells also experience different observation angles as seen from the antenna, which leads to large differences in antenna gain for each observed range cell. This must be compensated as well. These two effects are apparent from the radar equation which is shown in (11):

$$P_{rx}(x,y) = \frac{G_{tx}(x,y)G_{rx}(x,y)\lambda^2 A\sigma_0(x,y)}{(4\pi)^3 R^4(x,y)} P_{tx}. \tag{11}$$

Here, P_{rx} is the received power from a surface cell and P_{tx} is the transmitted power. G_{tx} and G_{rx} are the gains of the transmitting and receiving antenna, respectively. R indicates the range to an observed surface patch, while A is the surface area of the observed surface patch with a normalised radar cross section σ_0. Lastly, (x, y) indicates the surface cell location dependency of the variables in the equation, and λ is the wavelength at the radar's centre frequency. In this case, the 3D gain patterns of the SAR-1532-122-S2-DP antenna were obtained by performing electromagnetic simulations which were found to be in good agreement with the patterns reported in the data sheet.

To accomplish correction of the two effects, the total power returned by each surface cell for a surface is computed

using a numerical procedure described in [24]. This procedure works by discretizing a flat surface in many small cells, each having a corresponding area A. Subsequently, the observation angles, ranges, and incidence angles for the centre points of these surface cells are calculated using the equations in [24]. By setting the normalised radar cross section σ_0 and the transmitted power P_{tx} to 1, the power returned from each cell can be found, thus revealing the footprint of the antenna. This leads to equation (12):

$$P_0(x, y) = \frac{G_{tx}(x, y)G_{rx}(x, y)\lambda^2 A}{(4\pi)^3 R^4(x, y)}. \tag{12}$$

Therefore, the normalised radar cross section of a surface with unknown σ_0 can be found as shown in (13):

$$\frac{P_{rx}(x, y)}{P_0(x, y)P_{tx}} = \sigma_0(x, y). \tag{13}$$

As the range profile is defined as the total power received from all targets within a range bin, the range profile can be computed by summing the returned powers of each surface cell in the corresponding range bin. This procedure is mathematically shown in (14) where N is the number of range cells within a range bin l, with $P_{rx}(i)$ indicating the power returned by the i-th cell in the range bin.

$$P_{range}(l) = \sum_{i=1}^{N} P_{rx}(i) \tag{14}$$

Performing this summation is possible since the backscattered power originates from surface patches situated at different azimuth angles with respect to the transmitting antenna. As for typical grazing angles occurring in the automotive radar scenario the scattered power from the road surface is weak and preferably directed forwards, multiple scattering between surface patches located at the same range but at different azimuth angles can be neglected.

By using P_0 instead of P_{rx} in (14), the "normalised" range profile $P_{range,0}$ can be found. Since (14) is a linear operation, through its combination with (13), σ_0 can be found using (15) where $P_{range,measured}$ is the measured range profile by the radar.

$$\sigma_0(l) = \frac{P_{range,measured}(l)}{P_{range,0}(l)P_{tx}} \tag{15}$$

Since S-parameters describe field strengths instead of power as the RCS does, the measured S-parameters can be compensated for the antenna footprint by dividing them by the square root of the "normalised" range profile as shown in (16). Here, $S_{measured}$ are the measured S-parameters after performing steps IV-A to IV-C. Subsequently, the S-parameters can now be used to compute the coherency matrix and the $H\alpha A$ decomposition as described in section II.

$$S_{compensated}(l) = \frac{S_{measured}(l)}{\sqrt{P_{range,0}(l)}} \tag{16}$$

E. Averaging

In synthetic aperture radar, the averaging for obtaining the coherency matrix is usually performed in the spatial domain, meaning that surrounding pixels in the obtained imagery are grouped together to compute statistics. This can be expressed as shown in (17):

$$\langle x(k, l)\rangle = \sum_{i=k-N}^{k+N} \sum_{j=l-M}^{l+M} \frac{x(i, j)}{(2N+1)(2M+1)}. \tag{17}$$

In this equation, $\langle x(k, l)\rangle$ is the average of a quantity x of the cell at location (k, l). The parameters N and M define the window size along the two dimensions of the image while $x(i, j)$ is the value of quantity x in the cell with index (i, j). In this equation, x could for example be the backscattered power from a cell, or, in the case of computing the coherency matrix, an element from the target vector multiplied by its conjugate self.

In the automotive scenario, this type of averaging is less suitable. Namely, this would mean that a range-interval of the range profile is used for the averaging, which is not necessarily valid as this will contain backscattering from road surfaces observed at different angles of incidence. This is especially true for surface backscattering located at relatively short range from the radar. As the incidence angle plays an important role in the scattering behaviour of the rough surface, the range-interval will not contain samples from the same statistical process, thus leading to invalid estimated statistical properties in the coherency matrix.

However, the automotive scenario provides an opportunity to perform the averaging differently. Instead of averaging over space, the averaging can be performed over time. Namely, modern automotive radars transmit many chirps per second, so that averaging can take place over each obtained range profile. In this way, every range bin corresponds to backscattering from road surface under the same angle of incidence. Also, since the vehicle is moving, a different part of the road surface is encompassed by the antenna beam footprint, thus leading to samples independent from each other taken from the same statistical process. Mathematically, this can be formulated as:

$$\langle x(l)\rangle = \sum_{i=1}^{N} \frac{x_i(l)}{N}. \tag{18}$$

In (18), $\langle x(l)\rangle$ indicates the average of a quantity x in range bin l and $x_i(l)$ indicates the value of the quantity x in range bin l at measurement time index i. N is the number of measurements used to perform the averaging.

F. $H\alpha A$ Decomposition

The last step is computing the features from the coherency matrix as shown in (2) in combination with the averaging explained in section IV-E. This can be done using (3) to (7). Subsequently, the features can be plotted in various formats and be fed to a classifier for automatic classification.

V. Experimental Results

This section presents the results of applying the proposed pipeline to measurements in the laboratory, as well as those from measurements that took place outdoors.

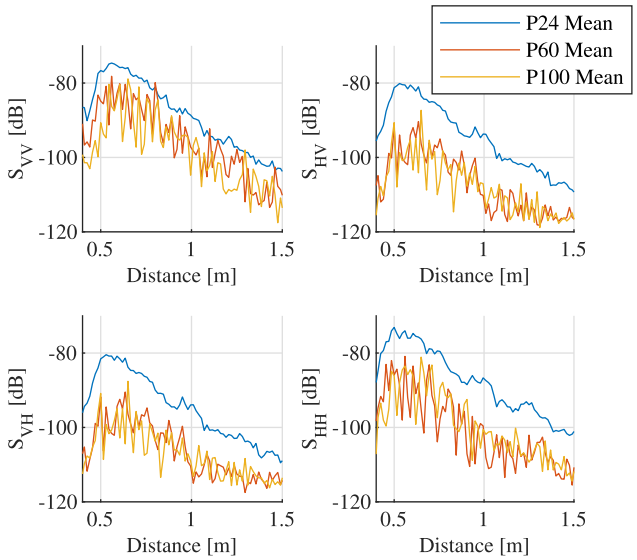

Fig. 6. Mean of measured S-parameters for the different types of sandpaper (P24, P60, and P100 in order of decreasing roughness) measured in lab conditions.

A. Lab Measurement Results

In Fig. 6 the mean value of the backscattered power from three different sandpaper samples in lab conditions is shown. It can be seen from this plot that there is clear distinction between the rough P24 type sandpaper and the smooth P60 and P100 sandpapers, while there does not seem to be a significant difference between the P60 and the P100 sandpaper. This is likely due to P60 type sandpaper already being too smooth to provide a significant backscattered contribution as the grain size in the sandpaper is relatively small compared to the wavelength. This is also the case for the P100 type sandpaper, leading to the observation that the backscattered radiation is caused by the sandpaper itself and/or the cavity that is formed between the backside of the sandpaper sample and the floor it was placed on.

Fig. 7 shows the results from the $H\alpha A$ decomposition, in particular the H and α features, graphed in the $H\alpha$-plane. In this plot, each symbol represents a range bin in the range of 0.5 to 1.5 metres. It can be seen that there is a clear difference between the P24 and the P100 type sandpapers. The P24 type shows a high entropy value whereas the P60 and P100 types show a broad spread but with centroids at lower values of entropy. The high entropy values indicate highly random scattering which is expected from a surface that differs electromagnetically from observation to observation. The lower entropy values of the smooth sandpaper types indicate less randomness in the scattering process. This can be explained by the grains of the sandpaper being too small compared to the wavelength. Therefore, from an electromagnetic point of few, a sheet of smooth sandpaper substrate material is measured, which is more or less the same from measurement to measurement. Fig. 6 reinforces this observation as it shows that the P60 and P100 types are indistinguishable from each other, thus also indicating that the grains on both sandpapers have become too small compared to the wavelength to contribute significantly to the backscattered power.

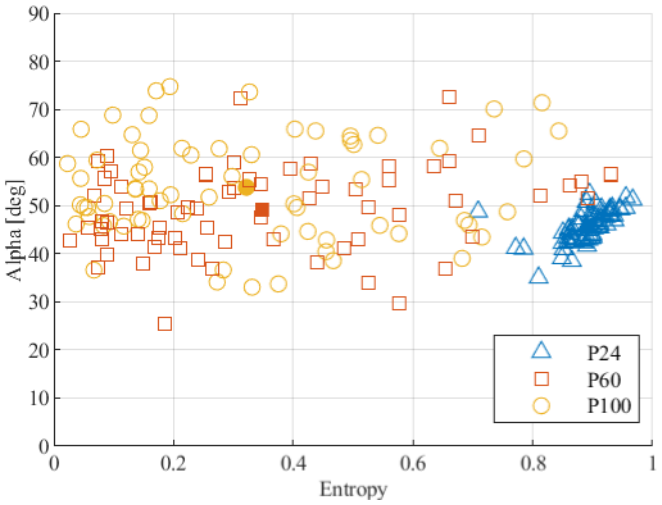

Fig. 7. The H and α features of the sandpaper measurements performed in the lab in the range interval from 0.5 to 1.5 metres. The solid coloured symbols indicate the clusters' centroids formed by the corresponding sandpaper types.

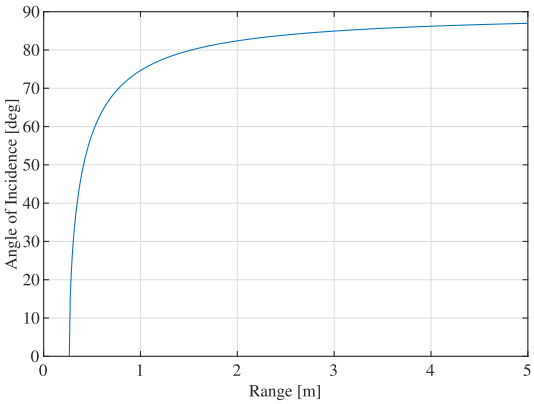

Fig. 8. The local angle of incidence at a point on the surface at a range indicated by the x-axis for an antenna height of 26.5 cm.

The unique geometry of the automotive scenario also allows for considering the H and α features as a function of range. The difference in range is related to the effective angle of incidence at the surface, where surface area close to the radar experiences a low angle of incidence (steep), and surface areas farther away experience a high angle of incidence (shallow). A plot of the variation of angle of incidence as function of range is shown in Fig 8.

As the angle of incidence can influence scattering properties, this can further help with distinguishing different surface classes. Fig. 9 shows the entropy as function of range. It can be seen that for the P24 type sandpaper, the entropy stays relatively constant as function of range, indicating that the same scattering mechanism is at play, independent of angle of incidence. However, for the P60 and P100 type, the entropy tends to increase as range increases, trending towards entropy values similar to the P24 measurements. This can be explained by the increased specularity at larger angles of incidence, leading to less backscattered power, in combination with the limited sensitivity of the VNA. Due to measured S-parameters being close to the noise floor as seen from Fig. 6, thermal noise takes over which results in high entropy values due to its random nature.

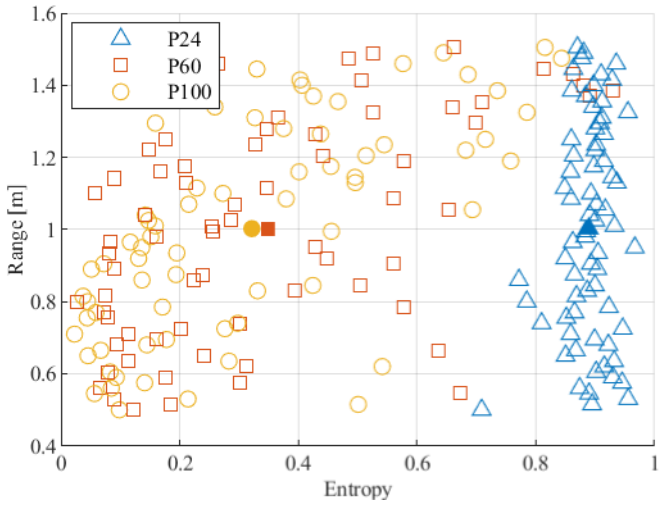

Fig. 9. The entropy feature of the different sandpaper types versus range, extracted from the experimental measurements. The solid symbols indicate the centroids of the clusters formed by each type of sandpaper.

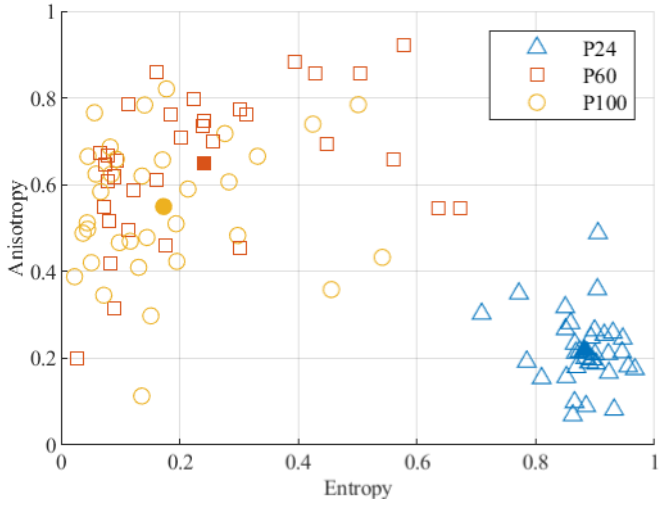

Fig. 10. The H and A features of the different sand paper types measured in a range interval from 0.5 to 1 metre. The solid symbols indicate the centroids of the clusters formed by each type of sandpaper.

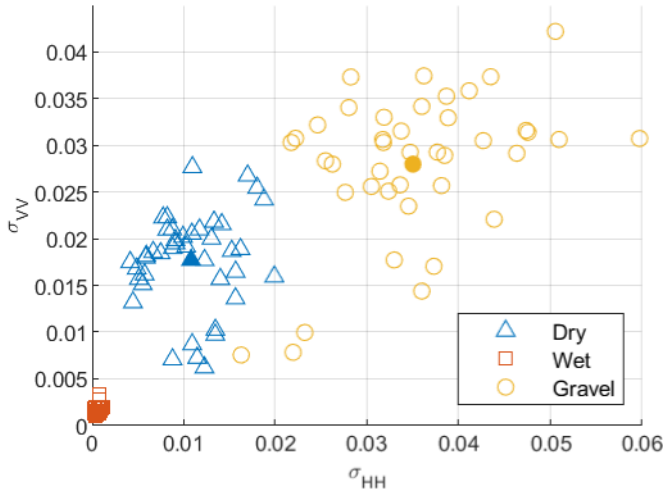

Fig. 11. Normalised radar cross sections in linear terms of the considered road surface conditions measured with a 60° orientation angle, in the range interval from 0.5 to 1.1 m.

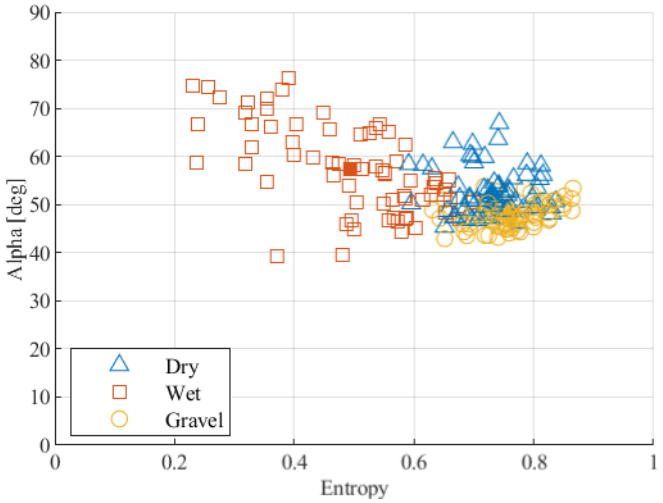

Fig. 12. The H and α features of the measurements performed outdoors in the range interval from 0.5 to 1.5 metres with an orientation angle of 60°. Here, the considered three surfaces are ordinary dry asphalt, wet asphalt, and asphalt covered by basalt stone gravel. The solidly coloured symbols indicate the centroids of the clusters formed by the measurements of the corresponding road surface conditions.

Finally, the anisotropy feature can be considered. The entropy versus anisotropy plot is shown in Fig. 10 for all ranges in the 0.5 to 1 meter interval. Here, a very clear distinction between the P24 and the other types of sandpaper can be seen, leading to the conclusion that the anisotropy is also useful for classification purposes in this case.

B. Outdoors Measurements Results

As seen from the lab measurements, rough surfaces can indeed be distinguished from smooth surfaces using the proposed pipeline. To evaluate if this method is also effective for actual road surfaces under various weather conditions, measurements on real road surfaces were performed. Fig. 11 shows the returned power after the averaging step, thus representing the normalised radar cross section of the surface. This measurement shows that for wet surfaces, the σ_{VV} is generally larger than σ_{HH}. However, as the roughness increases, σ_{HH} and σ_{VV} tend to become more equal, thus indicating depolarisation by a more diffusive scattering process due to the increased surface roughness as expected from theory.

Furthermore, the $H\alpha$-plane for all three road surface conditions (i.e., dry asphalt, wet asphalt, and asphalt covered in gravel) for a 60° orientation angle is shown in Fig. 12. It can be seen that there is a clear difference in the H and α features when comparing wet and dry road surface conditions. There also exists a small difference between road surface covered with basalt versus the regular road surface, however it is not as pronounced as with the road surface under wet conditions.

However, when taking the anisotropy into account as shown in Fig. 13, it can be seen that the separation between the basalt and the dry asphalt becomes larger, making it easier to separate these road surface conditions from each other.

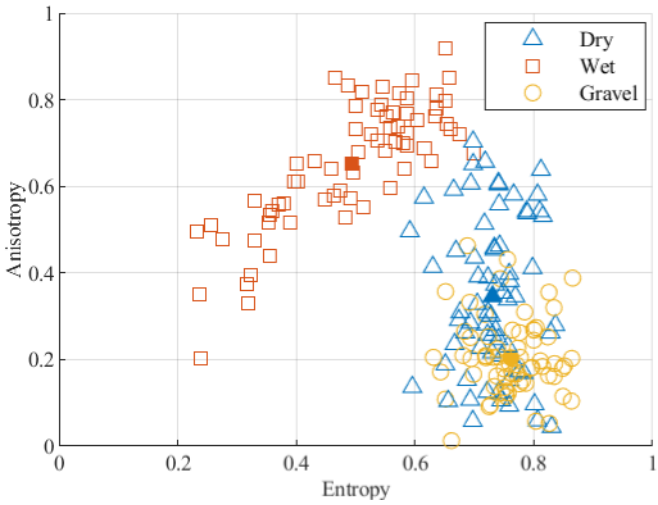

Fig. 13. The H and A features of the measurements performed outdoors in the range interval from 0.5 to 1.5 metres with an orientation angle of 60°. Here, the considered three surfaces are ordinary dry asphalt, wet asphalt, and asphalt covered by basalt stone gravel. The solidly coloured symbols indicate the centroids of the clusters formed by the measurements of the corresponding road surface conditions.

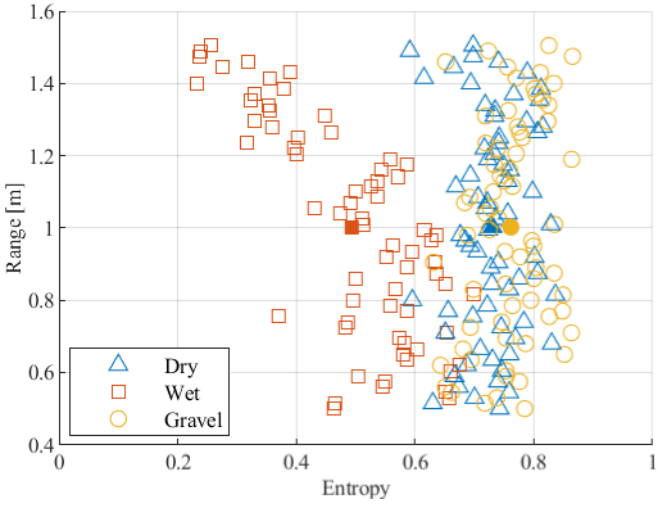

Fig. 14. The entropy versus range for the considered road surface conditions (i.e., asphalt which is dry, wet, and covered with basalt gravel), for an orientation angle of 60°. The solidly coloured symbols indicate the centroids of the clusters formed by the measurements of the corresponding road surface conditions.

Finally, the entropy, anisotropy, and α, can be considered as a function of range. Fig. 14 shows the entropy as a function of range. This figure shows that there is not much variation present in the entropy of regular asphalt and asphalt covered with basalt gravel, but that a range dependency is present for wet asphalt. This could be exploited by for example considering the H-values from 1.2 metres onward, resulting in more pronounced separation of the clusters of wet and dry conditions in the $H\alpha$-plane.

To quantify the loss in separation between the clusters, the euclidean distances between the centroids of the clusters is considered. The α feature was divided by 90° to ensure all features are within the same limits of 0 and 1. Furthermore, the standard deviations of all three features were computed as

TABLE II

EUCLIDEAN DISTANCE BETWEEN THE CENTROIDS AND STANDARD DEVIATIONS OF THE CLUSTERS FORMED BY THE H, α, AND A FEATURES OF DRY ASPHALT, WET ASPHALT, AND ASPHALT COVERED WITH GRAVEL, MEASURED IN A RANGE INTERVAL OF 0.5 TO 1.5 METRES WITH AN ANTENNA ORIENTATION ANGLE OF 60°

Dry	Wet	Gravel		σ H	σ α	σ A
0	0.39	0.15	Dry	0.054	0.053	0.179
	0	0.53	Wet	0.123	0.102	0.145
		0	Gravel	0.058	0.030	0.089

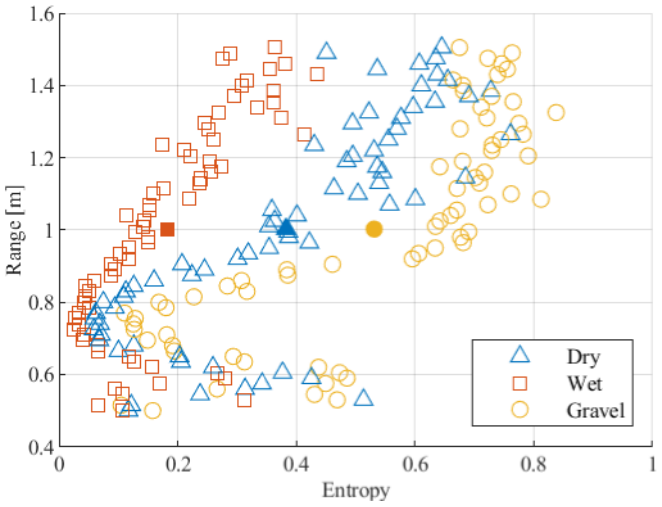

Fig. 15. The entropy versus range for the considered road surface conditions (i.e., asphalt which is dry, wet, and covered with basalt gravel), for an orientation angle of 90°. The solidly coloured symbols indicate the centroids of the clusters formed by the measurements of the corresponding road surface conditions.

an indication of the spread of the clusters in the $H\alpha A$ space. Table II lists the results of this with the distances between the clusters' centroids on the left side and the standard deviations of the three features on the right side.

Subsequently, the measurement results for an orientation angle of 90° can be considered. In Fig. 15 it can be seen that the entropy varies with range for all three different road surface conditions. When considering all range bins from 0.5 to 1.5 metres in the $H\alpha$-plane, this would result in potential overlap of the clusters of the different classes. However, when considering only measurements from 0.9 metres onward, the separation of the clusters is better. The results of this can be seen in Fig. 16 where only a selected spatial subset of the samples is used to form the plot with H and α features. A good separation of the clusters for the different surface conditions can be seen.

Finally, it is instructive to consider the anisotropy features obtained from the measurements as a function of range. It can be seen in Fig. 17 that the anisotropy does vary with range, but that it is more or less similar for each class. Therefore, for the set of measurements performed with an antenna orientation angle of 90°, the anisotropy is a less valuable feature compared with the results obtained at 60°.

Table III shows the distances between the centroids of the clusters, and the standard deviations of the road surface H, α, and A features performed with a measurement angle of 90°.

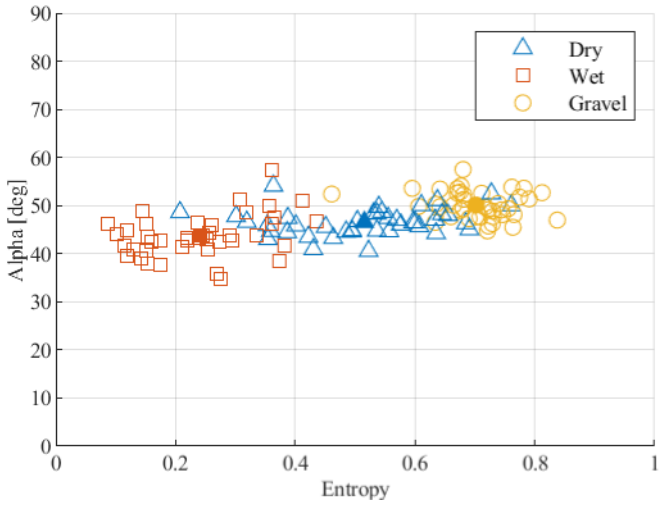

Fig. 16. The H and α features of the outdoor measurements in the range interval from 0.9 to 1.5 metres with an antenna orientation angle of 90°. The solidly coloured symbols indicate the centroids of the clusters formed by the measurements of the corresponding road surface conditions.

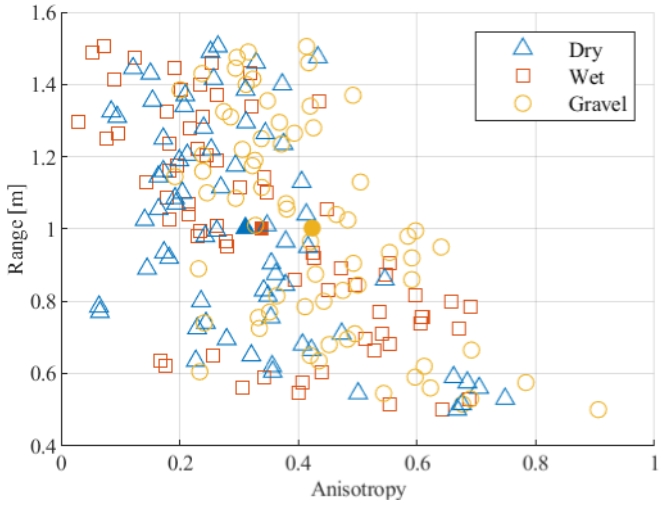

Fig. 17. Anisotropy versus range of the outdoor measurements performed with an orientation angle of 90°. The solidly coloured symbols indicate the centroids of the clusters formed by the measurements of the corresponding road surface conditions.

TABLE III

EUCLIDEAN DISTANCE BETWEEN THE CENTROIDS AND STANDARD DEVIATIONS OF THE CLUSTERS FORMED BY THE H, α, AND A FEATURES OF DRY ASPHALT, WET ASPHALT, AND ASPHALT COVERED WITH GRAVEL, MEASURED IN A RANGE INTERVAL OF 0.9 TO 1.5 METRES WITH AN ANTENNA ORIENTATION ANGLE OF 90°

Dry	Wet	Gravel		$\sigma\ H$	$\sigma\ \alpha$	$\sigma\ A$
0	0.28	0.23	Dry	0.126	0.031	0.095
	0	0.49	Wet	0.095	0.049	0.114
		0	Gravel	0.067	0.032	0.114

It can be seen that compared to the results measured with an orientation angle of 60° in table II, the distance between centroids has decreased, except for the distance between gravel and dry asphalt. Also, for the gravel, the spread of the cluster increased. However, for the other classes the spread remains similar except for the entropy spread of dry asphalt.

TABLE IV

EUCLIDEAN DISTANCE BETWEEN THE CENTROIDS AND STANDARD DEVIATIONS OF THE CLUSTERS FORMED BY THE CO- AND CROSS-POLAR RATIOS OF DRY ASPHALT, WET ASPHALT, AND ASPHALT COVERED WITH GRAVEL, MEASURED IN A RANGE INTERVAL OF 0.9 TO 1.5 METRES WITH AN ANTENNA ORIENTATION ANGLE OF 90°

Dry	Wet	Gravel		$\sigma\ \frac{\sigma_{VV}}{\sigma_{HH}}$	$\sigma\ \frac{\sigma_{HV}}{\sigma_{HH}}$	$\sigma\ \frac{\sigma_{VH}}{\sigma_{HH}}$
0	0.25	0.07	Dry	0.036	0.048	0.037
	0	0.32	Wet	0.197	0.187	0.200
		0	Gravel	0.008	0.027	0.021

To evaluate the results from the proposed pipeline, they are compared to results obtained using co- and cross-polarisation ratios as proposed in [16]. The used features are in this case σ_{VV}/σ_{HH}, σ_{VH}/σ_{HH}, and σ_{HV}/σ_{HH}. To compare the clusters formed by these features to those of the proposed pipeline, the polarisation ratios were normalised with the maximum value from all classes, so that all values are limited between 0 and 1 as would be done in a machine learning classifier. As these features are ratios of polarisation measurements, they are sensitive to noise. Namely, when σ_{HH} is small, noise may impact the ratios substantially and cause them to explode in value. To avoid this from occurring, only the range interval from 0.9 to 1.5 metres, which lies within the -10 dB antenna footprint, is considered. Subsequently, the same metrics are computed as for the H, α, and A features and are listed in table IV. Comparing these tables with each other, it can be seen that the distances between centroids is larger in all cases when using the proposed pipeline. Furthermore, the observation can be made that the clusters are smaller when using the ratio features for the dry and gravel classes, but the opposite is true for the wet asphalt class. Even though the dry and gravel classes have smaller standard deviations, this benefit is neglected as the centroids of these clusters are very close together. This suggests that the proposed pipeline is a robust alternative to classification based on simpler polarimetric ratios, as polarimetric ratios suffer from noise sensitivity and the normalisation usually performed for machine learning classifiers, which causes the clusters to be compressed close to the origin in the presence of outliers.

C. Polarisation Analysis

For the measurements previously presented, all four polarimetric channels were used. However, to reduce complexity and costs of an automotive radar system to be mass-produced, it may be advantageous to only partially measure the polarimetric response. To this extent, the results from the $H\alpha A$ decomposition are re-evaluated with the difference that the cross-polar channels are zeroed out. These channels can potentially be omitted as they contain less power than the co-polar channels as can be seen in Fig. 6.

The first observation that can be made on the effects of omitting the cross-polar channels is that this reduces the rank of the coherency matrix to two, as can be seen from (1) and (2). This in turn results in the coherency matrix only having two non-zero eigenvalues at maximum. Therefore, the anisotropy will be 1 as can be seen from (7), and thus will not contribute to separating road surface conditions.

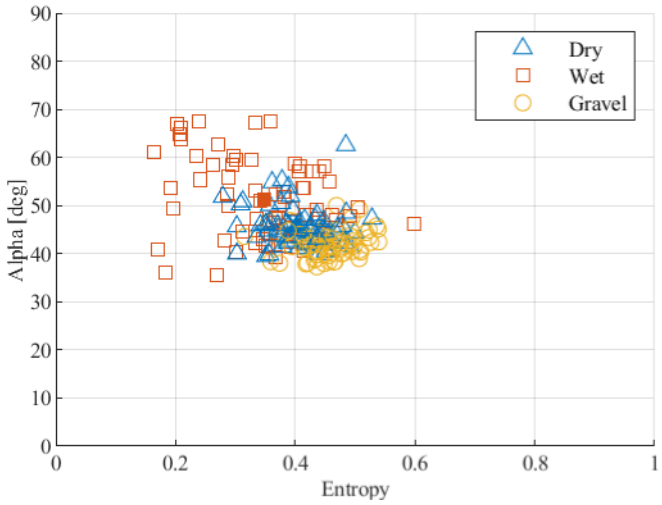

Fig. 18. The H and α features of the measurements performed outdoors in the range interval from 0.5 to 1.5 metres with an orientation angle of 60° with cross polar components zeroed out.

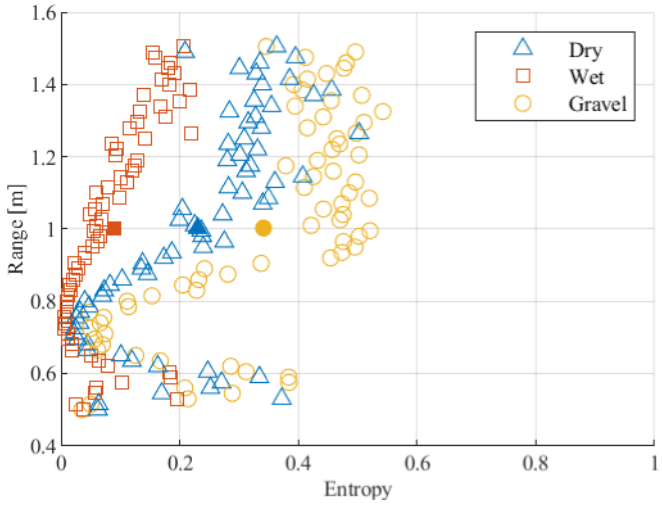

Fig. 19. The entropy versus range of the measurements performed outdoors with an orientation angle of 90° with cross polar components zeroed out.

Fig. 18 shows the effect of zeroing out the cross-polar channel on the positioning of surface reflections in the $H\alpha$-plane. When comparing this plot to that of Fig. 12, it can be seen that the wet road surface is still separated from the dry classes, but that this separation has decreased. Similarly, with measurements performed with an antenna orientation angle of 90°, the separation between different road surface conditions also decreases. This can be seen by comparing Figs. 15 and 19.

To quantify the loss in separation between the clusters for the measurements performed with an orientation angle of 60°, again the euclidean distances between the centroids and the standard deviation of the clusters are considered. Comparing table II and table V shows that the distances have decreased significantly, ranging from 59% to 78%. A similar comparison is shown for the measurements performed with an orientation angle of 90° in tables III and VI. Here, reductions of 30% to 34% can be seen. Thus, from these observations, it becomes clear that a radar system could be designed in such a way that the cross-polar channels are not measured at a cost of less separation between the clusters of several classes of road surface conditions. As the separation decreases, classification accuracy may see a reduction as well which leads to a trade-off between radar system complexity/costs and performance.

TABLE V

EUCLIDEAN DISTANCE BETWEEN THE CENTROIDS AND STANDARD DEVIATIONS OF THE CLUSTERS FORMED BY THE H, α, AND A FEATURES, COMPUTED WITH CROSS-POLAR COMPONENTS ZEROED OUT, OF DRY ASPHALT, WET ASPHALT, AND ASPHALT COVERED WITH GRAVEL, MEASURED IN A RANGE INTERVAL OF 0.5 TO 1.5 METRES WITH AN ANTENNA ORIENTATION ANGLE OF 60°

Dry	Wet	Gravel		σ H	σ α	σ A
0	0.08	0.06	Dry	0.052	0.045	0
	0	0.15	Wet	0.092	0.093	0
		0	Gravel	0.049	0.032	0

TABLE VI

EUCLIDEAN DISTANCE BETWEEN THE CENTROIDS AND STANDARD DEVIATIONS OF THE CLUSTERS FORMED BY THE H, α, AND A FEATURES, COMPUTED WITH CROSS-POLAR COMPONENTS ZEROED OUT, OF DRY ASPHALT, WET ASPHALT, AND ASPHALT COVERED WITH GRAVEL, MEASURED IN A RANGE INTERVAL OF 0.9 TO 1.5 METRES WITH AN ANTENNA ORIENTATION ANGLE OF 90°

Dry	Wet	Gravel		σ H	σ α	σ A
0	0.19	0.15	Dry	0.076	0.033	0
	0	0.34	Wet	0.056	0.053	0
		0	Gravel	0.047	0.037	0

VI. CONCLUSION

In this paper a novel processing pipeline incorporating the $H\alpha A$ decomposition for road surface condition identification in automotive scenarios has been proposed. An introduction to the $H\alpha A$ decomposition was presented to define the three features. Afterwards, the proposed pipeline was introduced, outlining a number of necessary steps to apply the decomposition in the context of automotive radar, such as the antenna footprint correction and the temporal averaging for the computation of the $H\alpha A$ polarimetric features.

Experimental measurements have been performed both in lab conditions on three different types of sandpaper (P24, P60, and P100) as well as outdoors on real road surfaces under various conditions. From the lab measurement results it could be seen that it is possible to distinguish rough and smooth sandpaper using the H, α, and A features. The rough sandpaper resulted in a dense cluster in the $H\alpha$-plane with a high entropy value while the smooth sandpapers showed on average a lower entropy value. Also, the smooth and rough sandpaper measurements were found to differ significantly in anisotropy: the rough sandpaper presented a low anisotropy while the smooth sandpapers showed a medium-high anisotropy.

The outdoor measurements were performed on three different road surface conditions, namely regular dry asphalt, wet asphalt, and asphalt covered by basalt gravel. All three road surface conditions were measured using antenna orientation angles of 60° and 90°. For both orientation angles, a clear difference exists between the wet and dry asphalt classes when

considering the H and α features. To further differentiate the dry asphalt from the asphalt covered with gravel in the 60° case, the anisotropy feature can be used. For the 90° orientation angle, the three road surface conditions can be distinguished in the $H\alpha$-plane. However, the anisotropy shows the same behaviour for all three classes.

The results of the proposed signal processing pipeline have been compared to classification based on features proposed in the literature, such as simple polarimetric ratios, by considering the distance in feature space between cluster centroids and the standard deviations of the features' values to keep the analysis as general as possible. This comparison shows that a larger separation of the clusters of samples from different road conditions could be achieved using the proposed pipeline. However, the clusters' centroids and standard deviations do not account for the cluster shapes and the complex multidimensional correlations that may exist within the distributions of features' values. These could potentially be exploited by classification algorithms and machine learning techniques to be explored in future work. Also, for future study it would be interesting to consider more comprehensive data sets to determine the effectiveness of the proposed pipeline for a greater variety of road surface conditions to evaluate its performance in the actual automotive scenario.

Finally, a polarimetric analysis was performed in which the importance of taking the cross-polar channels into consideration was evaluated by assessing the results when the cross-polar channel is zeroed out. Firstly, it was shown that the anisotropy feature can no longer be used in this case. Secondly, even if some separation between clusters was still observable, the cost of neglecting the cross-polar channels was found to be less separation of the different classes in the H, α, and A features. Namely, a reduction in cluster centroid separation of up to 78% for the measurements performed with an antenna orientation angle of 60° was observed, while a reduction of up to 34% was found for the 90° measurements. This likely leads to a decrease in classification accuracy. However, by not considering the cross-polar components, the radar systems can be reduced in complexity and cost.

ACKNOWLEDGMENT

The authors would like to thank F. van der Zwan and P. Swart for their help with the experimental measurements.

REFERENCES

[1] P. Hindle, "Comprehensive survey of 77, 79 GHz automotive radar companies—Sensors and ICs," *Microw. J.*, Mar. 2020. [Online]. Available: https://www.microwavejournal.com/articles/33705-comprehensive-survey-of-77-79-ghz-automotive-radar-companies-sensors-and-ics

[2] G. Hakobyan and B. Yang, "High-performance automotive radar: A review of signal processing algorithms and modulation schemes," *IEEE Signal Process. Mag.*, vol. 36, no. 5, pp. 32–44, Sep. 2019.

[3] E. Šabanovič, V. Žuraulis, O. Prentkovskis, and V. Skrickij, "Identification of road-surface type using deep neural networks for friction coefficient estimation," *Sensors*, vol. 20, no. 3, p. 612, Jan. 2020.

[4] P. Asuzu and C. Thompson, "Road condition identification from millimeter-wave radar backscatter measurements," in *Proc. IEEE Radar Conf.*, Apr. 2018, pp. 0012–0016.

[5] S. M. Sabery, A. Bystrov, P. Gardner, and M. Gashinova, "Surface classification based on low terahertz radar imaging and deep neural network," in *Proc. 21st Int. Radar Symp. (IRS)*, Oct. 2020, pp. 24–27.

[6] S. M. Sabery, A. Bystrov, P. Gardner, A. Stroescu, and M. Gashinova, "Road surface classification based on radar imaging using convolutional neural network," *IEEE Sensors J.*, vol. 21, no. 17, pp. 18725–18732, Sep. 2021.

[7] Y. Xiao, S. Cassidy, L. Daniel, S. Pooni, M. Cherniakov, and M. Gashinova, "Universal image segmentation framework on high-resolution automotive radar map," in *Proc. Int. Conf. Radar Syst. (RADAR)*, vol. 2022, Oct. 2022, pp. 226–231.

[8] S. R. Cloude and E. Pottier, "An entropy based classification scheme for land applications of polarimetric SAR," *IEEE Trans. Geosci. Remote Sens.*, vol. 35, no. 1, pp. 68–78, Jan. 1997.

[9] M. Martorella et al., "Target recognition by means of polarimetric ISAR images," *IEEE Trans. Aerosp. Electron. Syst.*, vol. 47, no. 1, pp. 225–239, Jan. 2011.

[10] G. Zhang et al., "Current status and future challenges of weather radar polarimetry: Bridging the gap between radar meteorology/hydrology/engineering and numerical weather prediction," *Adv. Atmos. Sci.*, vol. 36, no. 6, pp. 571–588, Jun. 2019.

[11] S. Trummer, G. F. Hamberger, R. Koerber, U. Siart, and T. F. Eibert, "Performance analysis of 79 GHz polarimetrie radar sensors for autonomous driving," in *Proc. Eur. Radar Conf. (EURAD)*, Oct. 2017, pp. 41–44.

[12] J. F. Tilly, O. Schumann, F. Weishaupt, J. Dickmann, and G. Waniliek, "Polarimetric information representation for radar based road user detection with deep learning," in *Proc. IEEE 24th Int. Conf. Inf. Fusion (FUSION)*, Nov. 2021, pp. 1–6.

[13] P. Beckmann and A. Spizzichino, *The Scattering of Electromagnetic Waves From Rough Surfaces* (International Series of Monographs on Electromagnetic Waves). Gosford, NSW, Australia: Pergamon Press, 1963.

[14] E. S. Li and K. Sarabandi, "Low grazing incidence millimeter-wave scattering models and measurements for various road surfaces," *IEEE Trans. Antennas Propag.*, vol. 47, no. 5, pp. 851–861, May 1999.

[15] J. Häkli et al., "Road surface condition detection using 24 GHz automotive radar technology," in *Proc. 14th Int. Radar Symp. (IRS)*, vol. 2, Jun. 2013, pp. 702–707.

[16] V. V. Viikari, T. Varpula, and M. Kantanen, "Road-condition recognition using 24-GHz automotive radar," *IEEE Trans. Intell. Transp. Syst.*, vol. 10, no. 4, pp. 639–648, Dec. 2009.

[17] A. Bystrov, E. Hoare, T.-Y. Tran, N. Clarke, M. Gashinova, and M. Cherniakov, "Automotive system for remote surface classification," *Sensors*, vol. 17, no. 4, p. 745, Apr. 2017.

[18] D. A. Bosma, O. A. Krasnov, and A. Yarovoy, "An advanced data processing algorithm for extraction of polarimetric radar signatures of moving automotive vehicles using the H/A/α decomposition technique," *Remote Sens.*, vol. 15, no. 4, p. 1060, Feb. 2023.

[19] V. Vassilev, "Road surface recognition at mm-wavelengths using a polarimetric radar," *IEEE Trans. Intell. Transp. Syst.*, vol. 23, no. 7, pp. 6985–6990, Jul. 2022.

[20] J.-S. Lee and E. Pottier, *Polarimetric Radar Imaging: From Basics to Applications*. Boca Raton, FL, USA: CRC Press, Jan. 2017.

[21] *WR-12 Waveguide Dual-Polarized Horn Antenna*. Accessed: Jan. 9, 2023. [Online]. Available: https://www.eravant.com/15-dbi-gain-60-to-90-ghz-45-db-isolation-wr-12-waveguide-e-band-dual-polarized-horn

[22] *Conversion Chart Abrasives—Grit Sizes*. Accessed: Nov. 16, 2022. [Online]. Available: https://www.fine-tools.com/G10019.html

[23] P. Leroux, "Sandpaper roughness measurement using 3D profilometry," Nanovea, Irvine, CA, USA, Tech. Rep., Jan. 2014.

[24] W. Bouwmeester, F. Fioranelli, and A. Yarovoy, "Dynamic road surface signatures in automotive scenarios," in *Proc. 18th Eur. Radar Conf. (EuRAD)*, Apr. 2022, pp. 285–288.

[25] W. Bouwmeester, F. Van Der Zwan, F. Fioranelli, and A. Yarovoy, "Dataset of fully polarimetric rough surface scattering from sandpaper and road surfaces in various conditions measured at 75 to 85 GHz," 4TU.ResearchData, Apr. 2023, doi: 10.4121/3DF8777A-3C9A-4A1F-A2D5-F487CA211897.V1.

[26] J. Dunsmore, "Gating effects in time domain transforms," in *Proc. 72nd ARFTG Microw. Meas. Symp.*, Dec. 2008, pp. 1–8.

Wietse Bouwmeester (Graduate Student Member, IEEE) received the B.Sc. degree in electrical engineering form the Delft University of Technology in 2016, and the M.Sc. degree in electrical engineering from the Delft University of Technology, with a focus on telecommunications and sensing systems. He graduated cum laude on the design of a conformal phased array antenna commissioned by ASTRON, the Dutch institute for radio astronomy. In May 2020, he joined the Microwave Sensing, Signals, and Systems group of the TU Delft as a Ph.D. candidate where he is currently working on polarimetric approaches to classify road surfaces and other targets with mm-wave radar for automotive applications.

Francesco Fioranelli (Senior Member, IEEE) received the Laurea (B.Eng., cum laude) and Laurea Specialistica (M.Eng., cum laude) degrees in telecommunication engineering from Università Politecnica delle Marche, Ancona, Italy, in 2007 and 2010, respectively, and the Ph.D. degree from Durham University, U.K., in 2014.

He was an Assistant Professor with the University of Glasgow from 2016 to 2019 and a Research Associate with University College London from 2014 to 2016. He is currently an Associate Professor with the Delft University of Technology (TU Delft), The Netherlands. He has authored over 140 publications between book chapters, journal and conference papers, edited the books on "micro-doppler radar and its applications" and "radar countermeasures for unmanned aerial vehicles" published by IET-Scitech in 2020. His research interests include the development of radar systems and automatic classification for human signatures analysis in healthcare and security, drones and UAVs detection and classification, automotive radar, wind farm, and sea clutter. He received three best paper awards.

Alexander G. Yarovoy (Fellow, IEEE) received the Diploma degree (Hons.) in radiophysics and electronics from Kharkov State University, Kharkiv, Ukraine, in 1984, and the Candidate Physics and Mathematical Sciences and Doctor Physics and Mathematical Sciences degrees in radiophysics, in 1987 and 1994, respectively. In 1987, he joined the Department of Radiophysics, Kharkov State University, as a Researcher and became a Full Professor in 1997. From September 1994 to 1996, he was with the Technical University of Ilmenau, Germany, as a Visiting Researcher. Since 1999, he has been with the Delft University of Technology, The Netherlands, where he has been leading as the Chair of the Microwave Sensing, Systems and Signals Group since 2009. He has authored and coauthored more than 450 scientific or technical articles, six patents, and 14 book chapters. His main research interests are in high-resolution radar, microwave imaging, and applied electromagnetics (in particular, UWB antennas). He was a recipient of the European Microwave Week Radar Award for the paper that best advances the state-of-the-art in radar technology in 2001 (together with L. P. Ligthart and P. van Genderen) and in 2012 (together with T. Savelyev). In 2010 together with D. Caratelli, he got the Best Paper Award of the Applied Computational Electromagnetic Society (ACES). He served as the General TPC Chair for the 2020 European Microwave Week (EuMW'20), as the Chair and the TPC Chair for the 5th European Radar Conference (EuRAD'08), and a Secretary for the 1st European Radar Conference (EuRAD'04). He also served as the Co-Chair and the TPC Chair for the Xth International Conference on GPR (GPR2004). He served as an Associate Editor for the *International Journal of Microwave and Wireless Technologies* from 2011 to 2018 and as a guest editor of five special issues of the IEEE TRANSACTIONS and other journals. From 2008 to 2017, he served as the Director of the European Microwave Association (EuMA).